Modeling of droplet breakup in a microfluidic T-shaped junction with a phase-field model

Mario De Menech[1,2,3]
[1]*Max-Planck Institut für Physik komplexer Systeme, Nöthnitzer Str. 38, 01187 Dresden, Germany*
[2]*Theoretische Physik, Fachbereich Naturwissenschaften, Universität Kassel, Heinrich-Plett-Str. 40, 34132 Kassel, Germany*
[3]*Unilever R&D Vlaardingen Olivier van Noortlaan 120, 3133 AT Vlaardingen, The Netherlands*
(Received 11 November 2005; published 30 March 2006)

A phase-field method is applied to the modeling of flow and breakup of droplets in a T-shaped junction in the hydrodynamic regime where capillary and viscous stresses dominate over inertial forces, which is characteristic of microfluidic devices. The transport equations are solved numerically in the three-dimensional geometry, and the dependence of the droplet breakup on the flow rates, surface tension and viscosities of the two components is investigated in detail. The model reproduces quite accurately the phase diagram observed in experiments performed with immiscible fluids. The critical capillary number for droplet breakup depends on the viscosity contrast, with a trend which is analogous to that observed for individual isolated droplets in hyperbolic flow.

DOI: 10.1103/PhysRevE.73.031505 PACS number(s): 47.11.−j, 47.60.+i, 47.55.D−, 47.55.Kf

I. INTRODUCTION

Much of the recent interest in the behavior of fluids in small channels stems from the wide range of applications that microfluidic devices are finding in biology and chemistry. The laminar regime of the flow in these systems allows an accurate control of mass and momentum transport, such that chemical species can be brought together in small quantities within restricted regions of space, enabling, for example, fast mixing [1] and high resolution of reaction kinetics [2]. In the case of two-phase systems, nanoliter and picoliter droplets can be handled with great precision when the destabilizing effects of wall impurities can be suppressed, producing well controlled structures [3–7]; partial wetting, in fact, introduces nonlinear instabilities which may generate complex erratic [7] or oscillatory patterns [8]. The variety of two-phase flow behaviors (see Fig. 1) is both interesting at a fundamental level and relevant for those applications based on the accurate tuning of droplet sizes [9]: microdroplets could, for example, be used to confine chemical reactions, or to deliver substances in well-defined amounts. Such a control is generally attainable for a limited range of flow conditions and with fluids having properties that are compatible with the surfaces of the device used. The combinations of materials, geometries and flow conditions which are being used in experimental setups are rapidly growing, and modeling can be extremely helpful both in providing insight and in improving the design and prototyping of microfluidic devices. In this respect, the main challenge of a modeling technique is to cope with the three dimensionality and the strong surface stresses present both at the fluid-fluid and fluid-solid interfaces.

Phase-field models have been developed for the study of the dynamics of critical phenomena, in particular in relation to nucleation and spinodal decomposition [10]. The spatial variations of the phase order parameter indicate the location of interfaces separating the growing domains, and interface coalescence and breakup is driven by the local curvature-dependent solubility (Gibbs-Thomson effect): interfacial regions of high curvature have a higher chemical potential which drives a mass flux to the surrounding medium to reduce the curvature and therefore the chemical potential gradients. The effects of fluid flow are included by adding an advection term to the diffusion equation of the order parameter, which is then coupled to a momentum transport equation to describe the hydrodynamics of a multiphase system [11,12]. From a computational point of view, modeling of fluid boundaries as having finite thickness greatly simplifies the handling of interface coalescence or breakup events, and in the case of phenomena occurring near the critical point, this approach is fully justified by the fact that, in the mean field approximation, interfaces are indeed diffuse, with a characteristic length which is comparable with the typical domain size. On the other hand, it can be shown that phase-field physics approaches asymptotically that of two immiscible fluids as the interface thickness becomes small compared to the local curvature, both for unbounded flow and in the presence of solid surfaces [13–15].

Phase-field models and a range of related numerical methods based on the generalized free-energy functional approach have been already applied to the modelling of droplet dynamics in unbounded flow or in the presence of solid boundaries, including droplet deformation and breakup [16–19], droplet formation [8] and spreading [20] on patterned surfaces. In this paper we use a phase-field model to study the three-dimensional flow of a binary mixture in constrained geometries in the hydrodynamic regime that characterizes the flow in microfluidic devices, i.e., with low Reynolds and capillary numbers. We show how the computed droplet flow and breakup dynamics in a T-shaped junction follows closely that observed experimentally for water in oil mixtures, despite the fact that the interface thickness in the simulations is far from the sharp-interface limit.

The paper is structured as follows: Section II describes in detail how the thermodynamic and transport properties of the nonhomogeneous system can be derived from a free-energy functional. The experienced reader may skip this part and move to the presentation of the results in the following sections. Section III presents the free-flow tests which were performed to validate the implementation of the code. The re-

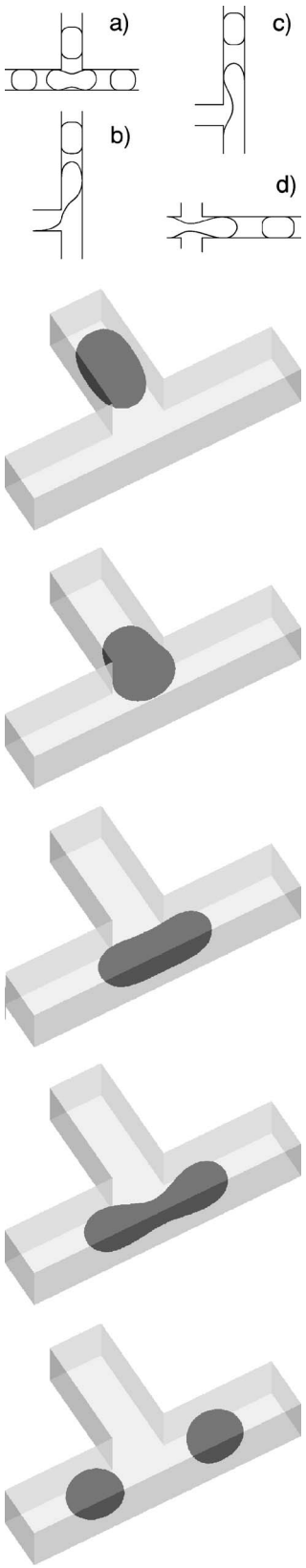

FIG. 1. Left, examples of simulations of two-phase flow dynamics in microfluidic devices: (a) droplet breakup in a symmetric T-junction; (b) and (c), droplet formation in a T-junction with cross flow; (d) droplet formation in a flow-focusing cross junction. Right, frames showing the modeled three-dimensional flow of a droplet in a symmetric T-junction with square cross section.

sults for the modeling of droplet flow and breakup at a T-shaped junction are reported in Secs. IV and V.

II. MODEL EQUATIONS

A unifying feature of all phase-field models is the existence of a free-energy functional, which, besides determining the equilibrium properties, strongly influences the dynamics of the system, whose transport equations can be derived from conservation arguments [12], or from generalized hydrodynamic theory [21]. In this section we briefly review this theoretical framework for a two-phase system, illustrating in particular how the surface tension, the wetting properties and the pressure tensor follow consistently from the choice of the free-energy functional.

A. Thermodynamics of the nonhomogeneous system

We consider a mixture of two fluids, A and B, with the Cahn-Hilliard-van der Waals form for the free energy in the volume V,

$$F[n,\varphi] = \int_V d\mathbf{r}\left(\frac{\kappa n}{2}|\nabla\varphi|^2 + nW(\varphi) + f(n)\right), \tag{1}$$

where $n=n_A+n_B$ is the total particle number density, $\varphi=n_B/n$ is the molar fraction of component B, κ determines the surface tension (see Sec. II B below) and f is the sum of the free-energy densities of the pure components, which for simplicity is assumed to depend only on the total density. Also, W is the free energy of mixing, for which we shall take the expression for a simple symmetric mixture [22],

$$W(\varphi) = 2kT_c\varphi(1-\varphi) + kT[\varphi\ln\varphi + (1-\varphi)\ln(1-\varphi)], \tag{2}$$

which is the sum of the ideal and the excess parts, k is Boltzmann's constant, and T and T_c are, respectively, the absolute and critical temperatures. The critical point corresponds to the molar fraction $\varphi_c=1/2$ and temperature T_c, so that below T_c the system phase separates; at $T=0$ the two components completely demix so that the equilibrium bulk molar fractions become $\varphi_A=0$ and $\varphi_B=1$. In the incompressible limit, $n=$const the equilibrium concentration satisfies the Euler-Lagrange equation

$$\mu(\mathbf{r}) = -\kappa\nabla^2\varphi(\mathbf{r}) + W'(\varphi(\mathbf{r})) = \mu_{\text{coex}}, \tag{3}$$

where $\mu(\mathbf{r})=\delta F/\delta\varphi(\mathbf{r})$ is the chemical potential difference, and μ_{coex} is the Lagrange multiplier which fixes the total molar fraction. For a flat interface $\mu_{\text{coex}}=0$ and φ is a function of one spatial coordinate only: the concentration profile varies between the equilibrium molar fractions φ_A and φ_B, within a region having a finite characteristic thickness ξ proportional to $\sqrt{\kappa/kT_c}$. In nonequilibrium conditions, local imbalances of the chemical potential $\mu(\mathbf{r})$ will generate diffusion currents which tend to restore the configuration satisfying Eq. (3).

B. Surface tension

The mechanical definition of surface tension for a flat interface is given by the integral of the difference between the normal and transverse pressures:

$$\sigma = \int_{-\infty}^{\infty} dx \left(P_{xx} - \frac{P_{yy} + P_{zz}}{2} \right), \tag{4}$$

where x is the direction normal to the interface. The pressure tensor must satisfy the Gibbs-Duhem equation (we consider only isothermal transformations)

$$\nabla_\beta \cdot P_{\alpha\beta} = n_A \nabla_\alpha \mu_A + n_B \nabla_\alpha \mu_B, \tag{5}$$

where $\mu_A = \delta F / \delta n_A$ and $\mu_b = \delta F / \delta n_B$ are the chemical potentials computed as functional derivatives of the free energy (1). The integrand in the functional (1) is a Lagrangian density, and is invariant under space translations; Noethers theorem can be applied to construct the expression for the associated conserved current [12], leading to the explicit form

$$P_{\alpha\beta} = \delta_{\alpha\beta}[nf'(n) - f(n)] + \kappa n \nabla_\alpha \varphi \nabla_\beta \varphi, \tag{6}$$

where we recognize the nonisotropic part [the second term in (6)] first introduced by Korteweg. From Eqs. (4) and (6), we get

$$\sigma = \int_{-\infty}^{\infty} dx \kappa n \left(\frac{d\varphi}{dx} \right)^2, \tag{7}$$

which corresponds to the excess energy with respect to the homogeneous system, also called the distortion energy [23]. For n=constant, the integral in (7) is easily expressed in terms of the mixing energy W,

$$\sigma = n \int_{\varphi_A}^{\varphi_B} d\varphi \sqrt{2\kappa \hat{W}(\varphi)}, \tag{8}$$

with $\hat{W}(\varphi) = W(\varphi) - W(\varphi_A) > 0$. Without loss of generality, we can set $\kappa = kT_c \xi^2$, so that the surface tension is $\sigma = kT_c n \xi \Omega$, with Ω given by the integral

$$\Omega = \int_{\varphi_A}^{\varphi_B} d\varphi \sqrt{2\hat{W}(\varphi)/kT_c}. \tag{9}$$

In the particular case $T=0$, the one-dimensional equilibrium molar fraction is $\varphi(x) = 1/2 + 1/2 \sin(2x/\xi)$ for $|x| < \pi\xi/2$, 0 or 1 otherwise. The interface width is $\pi\xi$ and the surface tension integral (9) gives $\Omega = \pi/4$. For $T > 0$ the bulk concentrations φ_A and φ_B of the flat interface profile are approached asymptotically, and the exact definition of ξ can be assigned in an arbitrary way. In this work ξ is defined as the interval over which the flat interface concentration rises from 34.4% to 65.6% of the total variation $\varphi_B - \varphi_A > 0$. In other terms, given the profile $\varphi(x)$, $\xi = |x_2 - x_1|$, where $(\varphi(x_1) - \varphi_A)/(\varphi_B - \varphi_A) = 1/2 - 1/2 \sin(1/\pi)$, $(\varphi(x_2) - \varphi_A)/(\varphi_B - \varphi_A) = 1/2 + 1/2 \sin(1/\pi)$. In the simulations reported here we choose $T/T_c = 0.8$, such that the mixing energy (2) is far from the singular limit $T=0$, and the interface thickness is still quite small.

C. Wetting

In the framework of the Cahn-Hilliard theory of diffuse interfaces, the interaction of the fluid components with a wall is introduced by adding to the functional (1) a surface energy term of the form [24]

$$F_s[n_A, n_B] = \int_V d\mathbf{r} \, \delta(S) \Phi(n_A, n_B), \tag{10}$$

where δ is Dirac delta function, $S(\mathbf{r}) = 0$ defines the locus of the points of the surface and Φ is the surface energy density. From the series expansion of Φ [23], we keep the first-order term only, $\Phi = -\kappa(G_A n_A + G_B n_B)$, with the coefficients G_A, G_B weighting the fluid-wall energy with respect to the same parameter κ governing the fluid-fluid surface tension of Eq. (7). In the incompressible case, surface energy variations depend only on the molar fraction φ and the difference $G = G_B - G_A$. The addition of the surface free energy (10) modifies the Euler-Lagrange equation (3) in the proximity of the wall and imposes a discontinuity in the gradient of φ,

$$-\kappa \nabla^2 \varphi + W'(\varphi) - \kappa G \delta(S) = \mu_{\text{coex}}; \tag{11}$$

the wall interaction is therefore included in the model as a boundary condition by simply imposing the constraint

$$\mathbf{n} \cdot \nabla \varphi = G, \tag{12}$$

where $\mathbf{n}$ is the normal to the wall surface, pointing inward to the solid. The parameter G, which has dimensions of 1/Length, determines the wetting of the solid by the two phases; $G > 0$ implies an attraction for component B, $G < 0$ a repulsion. As in the unbounded case of Eq. (3), the properties of one-dimensional solutions of Eq. (11) can be deduced from the first integral

$$\frac{\kappa}{2} \left(\frac{d\varphi}{dx} \right)^2 - \hat{W}(\varphi) = 0. \tag{13}$$

In particular, the equilibrium values φ_s of the molar fraction at the surface correspond to the solutions of

$$|G| = \sqrt{\frac{2}{\kappa} \hat{W}(\varphi)}, \tag{14}$$

and the solid-fluid surface energies σ_A and σ_B for the two phases are obtained as the sum of $-\kappa n G \varphi_s$ and the distortion energy integrals of the form (8) [23,25]. Together with the fluid-fluid surface tension σ, the surface energies σ_A and σ_B determine the static contact angle θ through Young's law, $\cos\theta = (\sigma_A - \sigma_B)/\sigma$.

D. Transport equations

The transport current for the density n_B ($n_A = n - n_B$, since we keep n constant) is the sum of an advection and a dissipative term, there the latter is proportional to the mobility Λ and the chemical potential gradient $\nabla\mu$. The fluid momentum equation, besides the nonlinear advection term, contains both reactive and dissipative forces, depending, respectively, on the pressure tensor and the shear viscosity η,

$$\frac{\partial n_B}{\partial t} = -\nabla \cdot (n_B \mathbf{v}) + \nabla \cdot (\Lambda \nabla \mu) \tag{15}$$

$$\frac{\partial \rho \mathbf{v}}{\partial t} = -\nabla \cdot \mathbf{P} - \nabla \cdot (\rho \mathbf{v}\mathbf{v}) + \nabla \cdot \eta[\nabla \mathbf{v} + (\nabla \mathbf{v})^T], \quad (16)$$

where ρ is the mass density and $\mathbf{v}$ is the mass average velocity. The isotropic part of the pressure stress tensor (6), $p = nf'(n) - f(n)$, is solved for by imposing the constraint $\nabla \cdot \mathbf{v} = 0$ rather than being derived by a specific form of the bulk free energy of the system. We will also take equal molar masses and a constant mobility for the two components, $\Lambda = Dn/kT$, with D the diffusion coefficient. The viscosity changes with the molar fraction, $\eta = \eta^* h(\varphi)$, and the following functional form is assumed for h:

$$h(\varphi) = \begin{cases} \left(\frac{\lambda - 1}{2\lambda}\right) \tanh\left(\frac{\varphi - 1/2}{\chi}\right) + \frac{\lambda + 1}{2\lambda} & \text{if } \lambda \geqslant 1, \\ \left(\frac{\lambda - 1}{2}\right) \tanh\left(\frac{\varphi - 1/2}{\chi}\right) + \frac{\lambda + 1}{2} & \text{if } \lambda < 1, \end{cases} \quad (17)$$

where $\lambda = \eta_B / \eta_A$ is the viscosity ratio and the parameter χ determines the sharpness of the transition of the viscosity as the phase separating interface is crossed; when $\chi \ll \varphi_B - \varphi_A$, we have that $\eta^* = \max\{\eta_A, \eta_B\}$ is the viscosity of the more viscous phase.

Given the unit time $\tilde{T}$, length $\tilde{L}$, mass $\tilde{M}$, and density $\tilde{n}$, we have the following dimensionless groups: Peclet number $\mathrm{Pe} = \tilde{L}^2 / D\tilde{T}$, Reynolds number $\mathrm{Re} = \tilde{\rho}\tilde{V}\tilde{L}/\eta^*$, Weber number $\mathrm{We} = \tilde{\rho}\tilde{V}^2\tilde{L}/\sigma$ and the Cahn number $C = \xi/\tilde{L}$, where $\tilde{V} = \tilde{L}/\tilde{T}$ is the unit velocity. We will maintain the symbols $\mathbf{v}$ and p of the dimensionless fields (p is rescaled with $\tilde{M}/\tilde{L}\tilde{T}^2$), W for the rescaled mixing energy $W\tilde{T}^2/\tilde{M}\tilde{L}^2$, t and ∇ for the dimensionless time and differential operator. The dimensionless transport equations become

$$\frac{\partial \varphi}{\partial t} = -\nabla \cdot (\varphi \mathbf{v}) + \frac{1}{\mathrm{Pe}} \nabla^2 [-C^2 \nabla^2 \varphi + W'(\varphi)], \quad (18)$$

$$\frac{\partial \mathbf{v}}{\partial t} = -\nabla \cdot (\mathbf{v}\mathbf{v}) - \nabla p - \frac{C}{\mathrm{We}\,\Omega} \nabla \cdot (\nabla \varphi \nabla \varphi) \quad (19)$$

$$+ \frac{1}{\mathrm{Re}} \nabla \cdot h[\nabla \mathbf{v} + (\nabla \mathbf{v})^T]. \quad (20)$$

The phase-field Navier-Stokes equations converge to the classical sharp interface behavior as the interface thickness, indicated by C, is reduced to zero along with the diffusivity $1/\mathrm{Pe}$ [14]. The mesh spacing used in the numerical solution imposes the main constraint on the Cahn number, since a sufficient number of points is needed to describe the interface profile in order to avoid spurious effects and to control the convergence of the solver. At finite C straining flows can thin or thicken the interface, and this must be resisted by diffusion, which therefore requires $1/\mathrm{Pe}$ to be high enough. On the other hand, too large a diffusion will overly damp the flow, which imposes a lower limit on the Peclet number. In our simulations, C and Pe, rather than being referred to the realistic values of an immiscible mixture such as water in oil, will therefore be chosen to optimize the approximation of the sharp interface physics, compatible with the limits imposed by the mesh size. Despite the fact that C will be typically as large as $1/20$ and Pe of the order 10, which is determined by the fact that we must deal with three-dimensional simulations, we will see that the model is capable of capturing the main features of droplet flow in simple microfluidic devices.

E. The numerical algorithm

The differential equations (18) and (20) are discretized on a uniform three-dimensional Cartesian grid with staggered velocities; the molar fraction and pressure fields are collocated at the centers of the cubic cells, while the velocity components are placed on the faces, and the boundaries of the simulated domain always coincide with a face of a grid cell, be it a wall, an inlet or a pressure outlet. The time evolution is implemented with a fully implicit Euler scheme, which is first order in time (see Appendix B).

III. FREE FLOW DYNAMICS

A. Spurious currents

The appearance of spurious currents in the proximity of the phase boundaries is a common feature shared by all numerical methods which include capillary stresses in the Navier-Stokes equation as a volume force to be computed on a grid [26]. A simple numerical test to illustrate their characteristics is to consider a droplet at rest; when the pressure and molar fraction fields are equilibrated, the velocity field is not zero, and parasite currents appear in the interface region, with a pattern which reproduces the symmetry of the underlying lattice (Fig. 2). The origin of the spurious currents can be explained by analyzing how the discretized form of the differential operators modifies the continuum transport equations (see Appendix A), and their magnitude grows with the coarseness of grid and the ratio between surface tension and viscosity. The magnitude of spurious currents can be most easily controlled by changing the lattice spacing. In our simulations the modulus of parasitic currents was kept below 5% of the characteristic velocity of the flow. This was achieved by choosing a lattice spacing which would be fine enough to maintain this degree of accuracy in the range of capillary numbers which were used.

B. Droplet deformation and breakup

Droplet deformation and breakup in unbounded simple shear flow depends on the ratio between droplet and matrix viscosities, $\lambda = \eta_d / \eta_c$, and the capillary number $\mathrm{Ca} = \eta_c \dot{\gamma} R / \sigma$ where $\dot{\gamma}$ is the shear rate and R is the radius. For low Ca, surface stresses are balanced by viscous ones and the droplet is stretched to a stationary ellipsoidal shape, with its principal axis following the direction of maximum elongation; the deformation is expressed in terms of Taylor's parameter $D = (L - B)/(L + B)$ [27], L being the long breadth of the drop, and B the small breadth [see inset to Fig. 3(a)]. The angle θ between the axis of maximum elongation and the shear direction gives the orientation of the droplet.

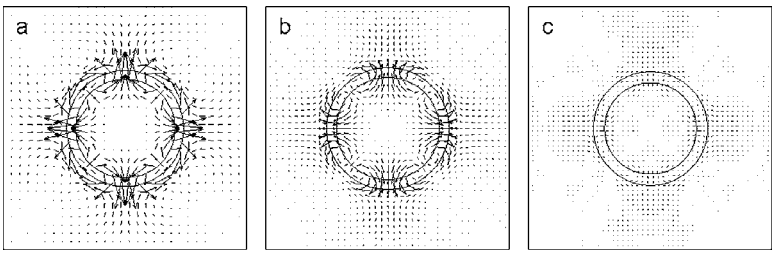

FIG. 2. Visualization of spurious currents for a static droplet relaxed on three different cubic meshes: (a) $\Delta x=C$, (b) $\Delta x=2C/3$, (c) $\Delta x=C/2$, $C=0.1$. The pressure, concentration, and velocity fields have reached the stationary state, and parasite currents persist in the proximity of the interface region indicated by the concentric circles. The spurious currents reflect the fourfold symmetry of the lattice, and depend on the size of the mesh. Measured in units of the reference velocity Re/We, the maximum spurious velocity decreases from 4×10^{-3} (a) to 2×10^{-3} (b), and 3×10^{-4} (c).

Simulation results are consistent with small deformation theories showing a linear relation between D and θ and Ca for $\mathrm{Ca}\ll1$ [Fig. 3(b)]. As the capillary number is increased above a critical value Ca_c, no steady shape exists and the droplet breaks. In our simulations, we find $0.4<\mathrm{Ca}_c<0.44$, in agreement with the value $\mathrm{Ca}_c\approx0.41$ obtained with more accurate numerical methods [28,29].

IV. DROPLET FLOW IN SQUARE MICROCHANNELS

As a first example of two-phase flow in a constrained geometry we discuss the pressure driven motion of droplets inside a channel having a square cross section. By choosing the appropriate value of the parameter G [Eq. (11)], the contact angle to the wall is set to zero, so that the continuous phase completely wets the boundaries. Exact results for droplet motion in capillaries are known only in the case of circular tubes [31]. In this case, theory shows that the speed of the drop U exceeds the average fluid speed by and amount UX, where $X\propto\mathrm{Ca}_T^{2/3}$, and $\mathrm{Ca}_T=\eta_c U/\sigma$ is the capillary number. In the case of square channels, to our knowledge, theoretical and experimental studies have been published only on the flow of bubbles, that is in the limit of small droplet viscosity $\eta_d\to0$ [32–35]. For viscous drops in square channels we verified that the value of λ strongly influences the droplet speed; at a given Ca_T the fractional velocity correction X increases as the viscosity ratio is decreased. We tested in particular the motion of droplets whose diameter is comparable with the channel width (Fig. 4), and verified that the values of X in the range $0.01<\mathrm{Ca}_T<0.2$ are consistent with the experimental results for bubbles by Thulasidas *et al.* [35], i.e., $0.3<X<0.45$.

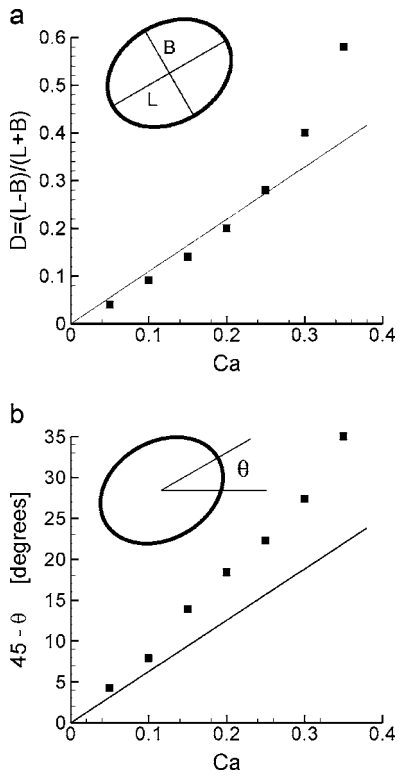

FIG. 3. Variation of deformation (a) and tilt angle (b) as a function of capillary number for a droplet in simple shear. The straight lines show the $\mathrm{Ca}\ll1$ limits derived by Taylor [27] and Chaffey and Brenner [30] ($\lambda=1$). The simulations were performed on a $80\times60\times60$ box with the top and bottom faces moving with opposite velocities parallel to the longer side. $C=\Delta x=0.05$.

V. DROPLET BREAKUP IN A T-JUNCTION

These simulations were motivated by the experiments by Link *et al.* [4] on droplet breakup in a T-shaped junction [6]. Isolated water droplets dispersed in an oil matrix are transported by a pressure-driven flow along a hydrophobic microchannel until they reach the junction, where they are stretched by the local elongational flow. Depending on the droplet size and relative strengths of viscous to capillary stresses, they split or simply flow without breaking down one of the two branches [see insets (a) and (b) in Fig. 5]. The dimensionless groups are the capillary number Ca_T, the viscosity ratio, $\lambda=\eta_d/\eta_c$ and the initial droplet extension $\varepsilon_0=l_0/\pi w_0$, where l_0 and w_0 are, respectively, the length and the diameter of the droplet upstream of the T-junction.

Figure 5 summarizes the results for two values of λ by reporting for each simulation a point with coordinates $(\varepsilon_0,\mathrm{Ca}_T)$; empty and filled symbols mark breaking and nonbreaking droplets, respectively. These two regions are separated by a curve whose shape can be derived with a general argument based on the Rayleigh-Plateau limit [4], and is given by the function

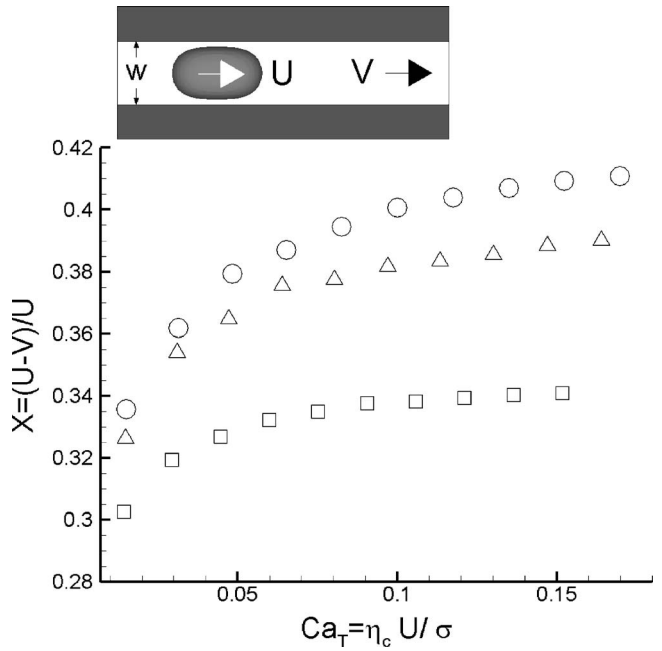

FIG. 4. Droplet flowing in a capillary with square cross section of width w; the (normalized) droplet excess speed is plotted against the capillary number for different viscosities: $\lambda=1/32$ (○), $\lambda=1/8$ (△), and $\lambda=1/2$ (□). U is the droplet speed while the V is average flow speed of the continuous phase (see inset). The undeformed radius of the droplet is $0.55w$. The simulation mesh is made by $125\times25\times25$ points, $C=\Delta x=0.04$.

$$\mathrm{Ca}_c = \alpha\varepsilon_0(1/\varepsilon_0^{2/3}-1)^2, \tag{21}$$

where $\alpha(\lambda)$ is a constant which depends on the viscosity contrast and the details of the geometry. We verified that this function describes very accurately the critical line for a range of λ. In particular we find $\alpha(1/8)=1.02\pm0.03$, $\alpha(1/2)=0.60\pm0.04$, $\alpha(1)=0.50\pm0.01$, $\alpha(3/2)=0.35\pm0.04$, $\alpha(2)=0.33\pm0.04$. These data clearly indicate that droplet breakup in the T-junction occurs more easily as the viscosity ration is increased, even when $\lambda>1$. The variation is quite rapid as the region around $\lambda=1$ is crossed, reaching a uniform value for large λ. Such behavior is in agreement with the viscosity dependence of the critical capillary number for an isolated droplet in a purely elongational flow [36]. Our result for $\alpha(1/8)$ closely agrees with the experimental value ($\alpha=1$) obtained with water droplets dispersed in hexadecane oil [4] (viscosity ratio $\lambda=1/8$), and is a demonstration of the accuracy of the numerical method presented here. As a final remark on the computational side, we would like to point outthat the position of the critical line remains quite consistent for different values of the Cahn number; Fig. 5 in fact reports data obtained for $C=1/15$ and $C=1/20$, showing how such relatively large values are sufficient to reproduce the critical boundary described by the function (21).

VI. CONCLUSIONS

We have discussed the application of a phase-field method to the modeling of immiscible two-phase flow in microfluidic devices in three dimensions; in particular, this approach is validated by investigating the dynamics of droplet breakup in a symmetric T-shaped junction. The phase diagram obtained from the numerical simulations agrees very closely with the experimental results which were performed with water-in-oil dispersions, confirming the reliability of the numerical approach. This conclusion was not guaranteed, given that the physics of the binary mixture approaches that of two immiscible fluids only in the limit of an interface thickness which is vanishingly small compared to the droplet size. Also, we were able to show that the resistance of the droplet to breakup depends on the viscosity ratio of the two fluids, following the characteristic trend of isolated droplets in a purely elongational flow.

The main advantage of the numerical method stems exactly from the fact that surface stresses are distributed over the finite interface thickness, allowing coarser meshes and therefore shorter simulation times. Furthermore, compared to other diffuse-interface models, the transport equations are

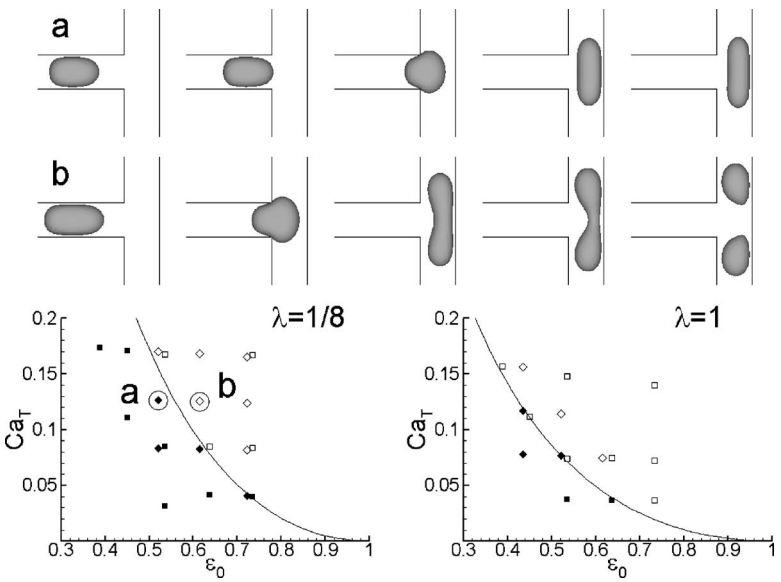

FIG. 5. Bottom, $(\varepsilon_0,\mathrm{Ca}_T)$ diagram summarizing the conditions for breaking drops at a symmetric T-junction for $\lambda=1/8$ (left) and $\lambda=1$ (right). Empty symbols correspond to nonbreaking droplets, filled symbols to breaking droplets; diamonds correspond to simulations preformed with $C=1/15$, while squares refer to simulations with $C=1/20$. The solid curves show the separating boundary from Eq. (21), with the viscosity dependent coefficients $\alpha(1/8)=1$ and $\alpha(1)=0.5$. 15×15 and 20×20 grid points were used for the square cross section, with Δx equal to $1/15$ or $1/20$, respectively. Re varied from 0.1 to 1. Top, the frames in (a) and (b) show the motion of droplets with different elongation and the same capillary number, corresponding to the points labeled a and b in the phase diagram for $\lambda=1/8$.

$---$}derived from a generalized free-energy functional, which determines also the equilibrium properties of the system, and is the starting point for extending the model to include more components and phases. The efficiency of the method, which we have shown does not come at the expense of accuracy or reliability, offers the possibility of handling two-phase flow in complex microfluidic devices; at the fundamental level, this should impact the understanding of phenomena related to droplet breakup and transport and pattern formation in such devices, and we may expect that implementations of the method will prove to be useful for design purposes.

ACKNOWLEDGEMENTS

The author would like to thank W. G. M. Agterof for useful discussions. The development of the code was supported by a Marie Curie Industrial Host Fellowship (HPMI-CT-1999-00017). Support form Unilever Corporate Research and the European Union (MRTN-CT-2004-005728) is also acknowledged. Special thanks to H. A. Stone and F. Jousse for their comments on the paper.

APPENDIX A: SPURIOUS CURRENTS

The origin of spurious currents can be explained by analyzing how the discretized form of differential operators modifies the continuum transport equations (18) and (20). Given set of stencil vectors $\{\mathbf{e}_i\}$ and the lattice spacing Δx, the action of $\hat{\boldsymbol{\nabla}}_\alpha$ and $\hat{\nabla}^2$ on a field $f(\mathbf{r})$ can be written in the general form

$$\hat{\boldsymbol{\nabla}}_\alpha f(\mathbf{r}) = \frac{1}{2\Delta x}\sum_i t_i f(\mathbf{r}+\Delta x\mathbf{e}_i)\mathbf{e}_{i\alpha}, \tag{A1}$$

$$\hat{\nabla}^2 f(\mathbf{r}) = \frac{1}{(\Delta x)^2}\sum_i t_i f(\mathbf{r}+\Delta x\mathbf{e}_i), \tag{A2}$$

where the coefficients $\{t_i\}$ are chosen to ensure the equality between the discretized and continuum operators to the leading order. Their values are obtained by expanding in Taylor series the term $f(\mathbf{r}+\Delta x\mathbf{e}_i)$ in Eqs. (A1) and (A2); for a stencil having inversion symmetry, the expansion contains only the lattice tensors with an even number of indices

$$T^{(2)}_{\alpha\beta} = \sum_i t_i \mathbf{e}_{i\alpha}\mathbf{e}_{i\beta}, \tag{A3}$$

$$T^{(4)}_{\alpha\beta\gamma\delta} = \sum_i t_i \mathbf{e}_{i\alpha}\mathbf{e}_{i\beta}\mathbf{e}_{i\gamma}\mathbf{e}_{i\delta}, \tag{A4}$$

$$\ldots,$$

and the effect of the anisotropy of the lattice on the actual expression of the differential operators depends on the invariance properties of the tensors $T^{(n)}$. In the case of the simple cubic stencil with the $6+1$ base vectors $\{\mathbf{e}_i\}=(\pm1,0,0),(0,\pm1,0),(0,\pm1,0)$ and $\mathbf{e}_0=(0,0,0)$, the values $t_0=0$ for the gradient, $t_0=-6$ for the Laplacian, and $t_{i=1,\ldots,6}=1$, imply that $T^{(2)}_{\alpha\beta}=2\delta_{\alpha\beta}$ is isotropic, such that $\hat{\boldsymbol{\nabla}}_\alpha f(\mathbf{r})=\boldsymbol{\nabla}_\alpha f(\mathbf{r})+O(\Delta x^2)$, and $\hat{\nabla}^2 f(\mathbf{r})=\nabla^2 f(\mathbf{r})+O(\Delta x^2)$. The coefficients of the fourth order tensor $T^{(4)}$, on the other hand, depend on the orientation of the stencil vectors with respect to the coordinate axis, and are responsible for the anisotropy effects in the discretized transport equations.

We now give a simple qualitative argument to relate the magnitude of the parasite currents to the dimensionless groups We, Re, and C and the lattice spacing Δx. Let us consider the example of the equilibrated droplet in absence of any external flow. The transport equations (18) and (20) are simplified to $\mu=$ const, $\nabla_\beta P_{\alpha\beta}=0$ and $\mathbf{v}=0$; in particular, the components F_α of the volume force are

$$F_\alpha = \boldsymbol{\nabla}_\alpha p + \frac{C}{2\,\mathrm{We}\,\Omega}\boldsymbol{\nabla}_\alpha|\boldsymbol{\nabla}\varphi|^2 + \frac{C}{\mathrm{We}\,\Omega}\nabla^2\varphi\boldsymbol{\nabla}_\alpha\varphi = 0 \tag{A5}$$

or

$$F_\alpha = \nabla_\alpha\tilde{p} + \frac{C}{\mathrm{We}\,\Omega}\nabla^2\varphi\boldsymbol{\nabla}_\alpha\varphi = 0, \tag{A6}$$

where we have redefined the isotropic pressure in the interface region, $\tilde{p}=p+(|\boldsymbol{\nabla}\varphi|^2/2)(C/\mathrm{We}\,\Omega)$. The discretized form of the volumetric force F_α is obtained with the replacement $\boldsymbol{\nabla}_\alpha\rightarrow\hat{\boldsymbol{\nabla}}_\alpha$, $\nabla^2\rightarrow\hat{\nabla}^2$ in Eq. (A6). When the fields $\tilde{p}^{(0)}$ and $\varphi^{(0)}$ solving equation (A6) for the equilibrated droplet are collocated on a grid, there is a residual stress of order $O(\Delta x^2)$ which depends explicitly on $T^{(4)}$:

$$\hat{F}_\alpha[\tilde{p}^{(0)},\varphi^{(0)}] = \Delta x^2\left(\frac{T^{(4)}_{\alpha\beta\gamma\delta}}{2\cdot 3!}\partial_{\beta\gamma\delta}\tilde{p}^{(0)} + \frac{C}{\mathrm{We}\,\Omega}(\partial_\alpha\varphi^{(0)})\frac{T^{(4)}_{\beta\gamma\delta\epsilon}}{4!}\partial_{\beta\gamma\delta\epsilon}\varphi^{(0)}\right) + O(\Delta x^4) \neq 0 \tag{A7}$$

and is balanced [neglecting the non linear advection term in (20)] by the shear stress produced by a nonzero velocity field $\mathbf{v}^{(1)}$, such that $\hat{F}_\alpha=\nabla^2 v^{(1)}_\alpha/\mathrm{Re}$. For the case of equal viscosities, given that $\tilde{p}^{(0)}$ in the interface region is proportional to $1/(\mathrm{We}\,C)$ and that each partial derivative introduces a factor $1/C$, the module of the spurious currents is estimated by the simple relation

$$v^{(1)} \propto \left(\frac{\Delta x}{C}\right)^2\frac{\mathrm{Re}}{\mathrm{We}}, \tag{A8}$$

and the proportionality factor depends on the noninvariant tensor $T^{(4)}$ which is responsible for the angular dependence of the parasite currents along the surface of the static droplet. Equation (A8) includes the main factors governing the magnitude of spurious currents, which are small for low surface tension or high viscosity, and can be controlled by including more grid points in the interface region, therefore decreasing the ratio $\Delta x/C$. This option is the most straightforward to use, at the cost of larger grids and therefore longer computational times. A more effective possibility consists in improving the symmetry properties of the discretization stencil

$\{\mathbf{e}_i\}$ by adding more vectors, such that the $T^{(4)}$ becomes isotropic and corrections are reduced to order $(\Delta x/C)^4$ [14].

APPENDIX B: THE NUMERICAL ALGORITHM

Given the array for the discretized fields at time step n, $\phi^n_{i=0,\ldots,3}=\varphi^n, v_1^n, v_2^n, v_3^n$, and p^n, their values at time step $n+1$ satisfy a set of equations of the form

$$\phi_i^{n+1} = \phi^n - \Delta t N_i(\phi_1^{n+1}, \phi_2^{n+1}, \phi_3^{n+1}, \phi_4^{n+1}, p^{n+1}), \quad \text{(B1)}$$

with the constraint of incompressibility, $\boldsymbol{\nabla}\cdot\mathbf{v}^{n+1}=0$. The explicit form of the nonlinear functions N_i is

$$N_0(\{\phi_i^{n+1}\}, p^{n+1}) = \hat{\boldsymbol{\nabla}}_\alpha(\varphi^{n+1}v_\alpha^{n+1}) - \frac{1}{\mathrm{Pe}}[-C^2\hat{\nabla}^4\varphi^{n+1} + \hat{\nabla}^2 W'(\varphi^{n+1})], \quad \text{(B2)}$$

$$N_\alpha(\{\phi_i^{n+1}\}, p^{n+1}) = \hat{\boldsymbol{\nabla}}_\beta(v_\alpha^{n+1}v_\beta^{n+1}) + \hat{\boldsymbol{\nabla}}_\alpha p^{n+1} + \frac{C}{\mathrm{We}\,\Omega}\hat{\boldsymbol{\nabla}}_\beta(\hat{\boldsymbol{\nabla}}_\alpha\varphi^{n+1}\hat{\boldsymbol{\nabla}}_\beta\varphi^{n+1}) - \frac{1}{\mathrm{Re}}\hat{\boldsymbol{\nabla}}_\beta[h(\hat{\boldsymbol{\nabla}}_\alpha v_\beta^{n+1} + \hat{\boldsymbol{\nabla}}_\beta v_\alpha^{n+1})], \quad \text{(B3)}$$

$$\alpha = 1,2,3,$$

and the operators $\hat{\boldsymbol{\nabla}}_\alpha$ refer to the finite-difference approximations of the partial derivative operators. The iterative scheme for the completion of the time step goes as follows:

(1) Given the current guess of the new values for the fields, ϕ_i^* and p^*, which at the beginning of the iteration loop will be simply ϕ_i^n and p^n, Eqs. (B1) are solved in sequence to get the new guesses ϕ_i^{**},

$$\varphi^{**} = \varphi^n - \Delta t N_1(\varphi^{**}, v_1^*, v_2^*, v_3^*, p^*), \quad \text{(B4)}$$

$$v_1^{**} = v_1^n - \Delta t N_2(\varphi^{**}, v_1^{**}, v_2^*, v_3^*, p^*), \quad \text{(B5)}$$

$$v_2^{**} = v_2^n - \Delta \tau N_3(\varphi^{**}, v_1^{**}, v_2^{**}, v_3^*, p^*), \quad \text{(B6)}$$

$$v_3^{**} = v_3^n - \Delta \tau N_4(\varphi^{**}, v_1^{**}, v_2^{**}, v_3^{**}, p^*). \quad \text{(B7)}$$

Each inner iteration is solved recursively by substituting $\phi^{**} \simeq \phi_{k+1} = \phi_k + \delta_k$ with $\phi_0 = \phi^n$ and linearizing in δ_k.

(2) The continuity equation, is enforced with a prediction-correction method (see, for example, Ref. [37]), leading to new values v_i^{***} and p^{**},

(3) The outer iteration is completed by setting $\varphi^{**} \to \varphi^*$, $v_i^{***} \to v_i^*$, $p^{**} \to p^*$, and computing of the residuals

$$R_i(\phi_i^*) = \phi_i^n - \phi_i^* - N_i(\{\phi_i^*\}, p^*), \quad i = 0,1,2,3 \quad \text{(B8)}$$

together with the divergence field $D=\hat{\boldsymbol{\nabla}}\cdot u^*$; the outer iteration loop is completed if $\|R_0(\varphi^*)\| < \epsilon\|\varphi^*\|$ and $\|R_i(\varphi^*)\| < \epsilon\|v^*\|$, $i=1,2,3$, and $\|D\| < \epsilon$, are all satisfied. In all simulations presented in this paper we set $\epsilon = 10^{-5}$. When the desired accuracy is reached, the new fields are obtained by setting $\phi_i^{n+1} = \phi_i^*$, $p^{n+1} = p^*$.

Besides the periodic boundaries used for the case of unbounded flow, we can handle walls, inlets and outlets. For all three kinds of boundaries the normal gradient of the chemical potential is set to zero ($\mathbf{n}\cdot\boldsymbol{\nabla}\mu = 0$). The boundary conditions (BC) at the walls include the constraint (12) for the molar fraction, the no-flow conditions $\mathbf{n}\cdot\boldsymbol{\nabla}p = 0$ and $\mathbf{v}_\perp = 0$, and the no-slip condition $\mathbf{v}_\parallel = \mathbf{v}_{\mathrm{wall}}$, where $\mathbf{v}_{\mathrm{wall}}$ is the tangential velocity of the wall. Inlets have Dirichlet BC for the molar fraction and velocity and Neumann BC for the pressure ($\varphi = \mathrm{const}, \mathbf{v}_\perp = \mathrm{const}, \mathbf{v}_\parallel = 0, \mathbf{n}\cdot\nabla p = 0$), while outlets have the complementary setup ($\mathbf{n}\cdot\nabla\varphi = 0, \mathbf{n}\cdot\nabla\mathbf{v} = 0, \mathbf{v}_\parallel = 0, p = \mathrm{const}$).

[1] J. B. Knight, A. Vishwanath, J. P. Brody, and R. H. Austin, Phys. Rev. Lett. **80**, 3863 (1998).
[2] C. N. Baroud, F. Okkels, L. Menetrier, and P. Tabeling, Phys. Rev. E **67**, 060104(R) (2003).
[3] S. Anna, N. Bontoux, and H. A. Stone, Appl. Phys. Lett. **82**, 364 (2003).
[4] D. R. Link, S. L. Anna, D. A. Weitz, and H. A. Stone, Phys. Rev. Lett. **92**, 054503 (2004).
[5] A. M. Ganán-Calvo and J. M. Gordillo, Phys. Rev. Lett. **87**, 274501 (2001).
[6] T. Thorsen, R. W. Roberts, F. H. Arnold, and S. R. Quake, Phys. Rev. Lett. **86**, 4163 (2001).
[7] R. Dreyfus, P. Tabeling, and H. Willaime, Phys. Rev. Lett. **90**, 144505 (2003).
[8] O. Kuksenok, D. Jasnow, J. Yeomans, and A. C. Balazs, Phys. Rev. Lett. **91**, 108303 (2003).
[9] M. Joanicot and A. Ajdari, Science **309**, 887 (2005).
[10] J. W. Cahn, J. Chem. Phys. **42**, 93 (1965).
[11] P. C. Hohenberg and B. I. Halpering, Rev. Mod. Phys. **49**, 436 (1977).
[12] D. M. Anderson, G. B. McFadden, and A. A. Wheeler, Annu. Rev. Fluid Mech. **30**, 139 (1998).
[13] R. Chella and J. Viñals, Phys. Rev. E **53**, 3832 (1996).
[14] D. Jacqmin, J. Comput. Phys. **155**, 96 (1999).
[15] D. Jacqmin, J. Fluid Mech. **402**, 57 (2000).
[16] A. J. Wagner and Y. M. Yeomans, Int. J. Mod. Phys. C **8**, 773 (1997).
[17] A. J. Wagner, L. M. Wilson, and M. E. Cates, Phys. Rev. E **68**, 045301(R) (2003).
[18] V. E. Badalassi, H. D. Ceniceros, and S. Banerjee, J. Comput. Phys. **190**, 371 (2003).
[19] J. Kim, J. Comput. Phys. **204**, 784 (2005).
[20] A. Dupuis and J. M. Yeomans, FGCS, Future Gener. Comput. Syst. **20**, 993 (2004).
[21] P. M. Chaikin and T. C. Lubensky, *Principles of Condensed Matter Physics* (Cambridge University, Cambridge, 1995).
[22] J. M. Prausnitz, R. N. Liechtenthaler, and E. G. de Azevedo, *Molecular Thermodynamics of Fluid-Phase Equilibria* 2nd ed.

(Prentice-Hall, New York, 1986), Chap. 6.
[23] P. G. de Gennes, Rev. Mod. Phys. **57**, 827 (1985).
[24] J. W. Cahn, J. Chem. Phys. **66**, 3667 (1977).
[25] P. Seppecher, Int. J. Eng. Sci. **34**, 977 (1996).
[26] R. Scardovelli and S. Zaleski, Annu. Rev. Fluid Mech. **31**, 567 (1999).
[27] G. I. Taylor, Proc. R. Soc. London, Ser. A **138**, 41 (1932).
[28] J. M. Rallison, Annu. Rev. Fluid Mech. **109**, 465 (1981).
[29] J. Li, Y. Y. Renardy, and M. Renardy, Phys. Fluids **12**, 269 (2000).
[30] C. Chaffey and H. Brenner, J. Colloid Interface Sci. **24**, 258 (1967).
[31] S. R. Hodges, O. E. Jensen, and J. M. Rallison, J. Fluid Mech. **501**, 279 (2004).
[32] W. B.Kolb and R. L. Cherro, Phys. Fluids A **5**, 1549 (1993).
[33] H. Wong, C. Radke, and S. Morris, J. Fluid Mech. **292**, 71 (1995).
[34] H. Wong, C. Radke, and S. Morris, J. Fluid Mech. **292**, 95 (1995).
[35] T. C. Thulasidas, M. A. Abraham, and R. L. Cherro, Chem. Eng. Sci. **50**, 183 (1995).
[36] B. J. Bentley and L. G. Leal, J. Fluid Mech. **167**, 241 (1986).
[37] P. Wesseling, *Principles of Computational Fluid Dynamics*, No. 29 in Springer Series in Computational Mathematics (Springer-Verlag, Berlin, Heidelberg, 2001).